Extending the Modified Transverse Crack Tensile test for Mode II Fracture Toughness Characterisation of Hybrid Interfaces

Tommaso Scalici[1]*, Denis Dalli[2,3], Zahur Ullah[4], Giuseppe Catalanotti[1]

[1] Dipartimento di Ingegneria e Architettura - Mediterranean Aeronautics Research & Training Academy (M.A.R.T.A)
University of Enna "Kore", Polo scientifico e tecnologico di Santa Panasia, Enna, 94100, Italy

[2]DEMec, Faculdade de Engenharia, Universidade do Porto, Rua Dr. Roberto Frias, 4200-465, Porto, Portugal

[3]INEGI, Instituto de Ciência e Inovação em Engenharia Mecânica e Engenharia Industrial, Rua Dr. Roberto Frias, 400, 4200-465 Porto, Portugal

[4] Department of Engineering, Durham University, South Rd, DH1 3LE Durham, UK

**Corresponding Author*

Abstract

Measuring mode II fracture toughness at a dissimilar interface using the Transverse Crack Tensile may be challenging, particularly if geometric and elastic symmetry conditions are not maintained during crack propagation. Building on previous results, the authors propose to extend the modified Transverse Crack Tensile test setup to hybrid interfaces. A preliminary parametric calibration was carried out to determine key design parameters. The proposed method was experimentally validated through mechanical testing with the assistance of DIC to evaluate the full-field strain. A Finite Element model was appropriately implemented to study the extension of potential plastic zones. The results obtained for the chosen metal-composite interface demonstrate that the proposed test setup can be successfully extended to hybrid interfaces, confirming its robustness. Additionally, guidelines for the design of the test samples are provided.

Keywords: Delamination, Hybrid Composites, Fibre Metal Laminates, Experimental methods.

1. Introduction

The last decades have seen a marked increase in the use of composite materials in the transportation sector. Their superior strength-to-weight performance enabled the design of lighter structures, resulting in air and terrestrial vehicles offering significantly reduced emissions and energy consumption [1–3]. However, due to the intrinsic material complexity and associated design uncertainty, certification authorities expect composite components to meet more stringent standards. This often results in over-dimensioning practices that compromise the true weight-saving potential of composites. For this reason, academia, research centres and industry have committed to study and develop new, reliable, and robust methods to precisely describe and measure the mechanical response and failure mechanisms that characterise composite materials [4,5] thus providing greater confidence in the design of composite structures.

While manufacturing flexibility gives composite engineers the possibility of designing monolithic components, larger structures are typically made from numerous joined parts to limit complexity, reliability, manufacturing, maintenance, and logistical issues. As in the case of metal components, mechanical fasteners usually represent the current "*best practice*" solution for joining composite parts, even if novel fastener-free through-thickness reinforced joints are starting to attract increased attention [6]. However, mechanical fastening guarantees joint reversibility, allowing for easier disassembly, improved inspectability and repairability, and the replacement of limited portions of the structure in case of irreversible damage, with a substantial maintenance cost reduction. On the other hand, using mechanical fasteners in combination with composite laminates may be insidious. In the first instance, composites lack the plasticity characteristic of metals, and this may lead to a sudden failure of the joint before any detectable warning signs, thus creating a clear safety issue. Moreover, composites are characterised by various failure mechanisms (e.g. fibre fracture, fibre kinking, matrix cracking, delamination) and a high notch sensitivity, and their performance is strongly influenced by both geometry and laminate layup, making failure prediction extremely challenging. Furthermore, Additionally, highly orthotropic composite joints typically suffer from low bearing and shear strengths.

To overcome some of these issues, the laminate can be locally thickened in the area surrounding the joint, thus lowering the stress levels in these critical zones. Additional plies can also be locally introduced to enhance material quasi-isotropy. However, ply drop-offs, and the one-sided laminate eccentricity resulting from local thickening, may introduce spurious and undesirable stresses. Moreover, this approach can lead to increased fastener dimensions and overall weight, thus undermining the joint efficiency [7–10].

Several methods have already been proposed to enhance the behaviour of mechanically-fastened joints [11–14], yet often their complexity has inhibited them from finding industry-wide applications. The most promising approach involves the use of hybridised fibre metal laminates (FML), such as local interleaving of the composite with metal foils. Various authors investigating FML demonstrated a remarkable increase in joint bearing strength, as well as the possibility to exploit the plasticity of the metal foil. Furthermore, FML hybridisation employing a ply-substitution method prevents the local thickening of the composites. Recent improvements in metal surface treatments and new manufacturing techniques further support the interest in this solution [15–17].

In the typical design of a locally interleaved joint, three main zones can be identified: a fully hybrid region, characterised by alternating composite plies and metal foils, homogeneous through the entire thickness, that is directly subjected to the load transferred by the fastener, and to which the enhancement of the joint performance is mainly attributable (enhanced bearing strength, fatigue behaviour, energy absorption); a monolithic FRP region that usually constitutes the largest part of the component, and which is meant to support the global loads; a transition region where the number of metal layers is gradually adjusted (Figure 1).

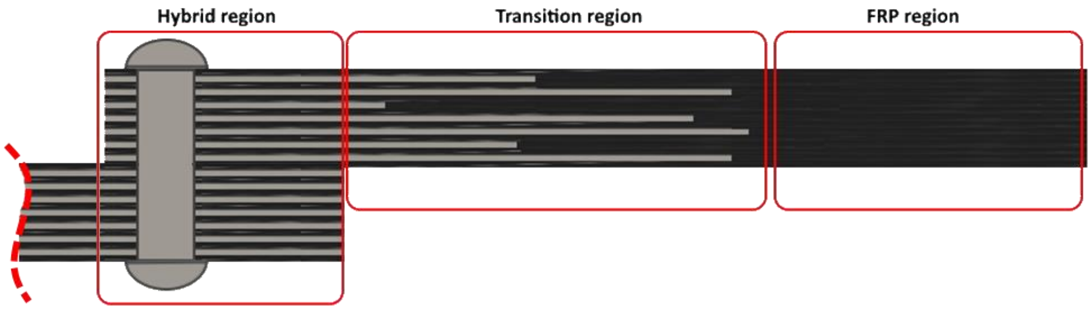

Figure 1 – Schematic representation of a locally hybridised bolted sample (after Camanho et al. [17]**).**

The transition and hybrid regions are both prone to hybrid interface delaminations. Interlaminar failure may initiate from the stress concentrations localised at the metal-composite ply substitution zones or at the fastener hole itself. Thus, hybrid interface interlaminar properties become essential input parameters for the numerical models used in the design of such hybrid joints. In such a mechanically fastened joint, the presence of the bolt constrains the relative opening movement of the plies, thus managing to suppress most mode I interlaminar failure propagations, leaving mode II as the predominant failure mode. The more proximate the interlaminar failure is to the fastener, the stronger the mode II dominance [18–20].

For the measurement of mode II fracture toughness, several authors have made use of the standardised End Notched Flexure (ENF) [21–23] and End Loaded-Split (ELS) [24–26] tests when characterising monolithic composites. After comparing different variants of these two tests, including a number of standard and non-standard data reduction techniques, Pérez-Galmés et al. [24] concluded that the Calibrated ELS test method was the most suitable method. However, hybrid interfaces present a different challenge for mode II characterisation which has not yet been addressed. The data reduction techniques suitable for standard ENF and ELS coupon tests do not allow for different stiffnesses in the two arms. Testing coupons in which substrates have different stiffnesses results in fracture propagation that is not purely mode II [27,28]. However, Hwang et al. [29] pointed out that the compliance method [23] is not recommended in the case of hybrid composite samples. Nevertheless, Mujika et al. [30] reported that the compliance calibration method can be used to determine the pure mode II ERR if certain conditions are respected in designing multimaterial Asymmetric-ENF. On the other hand, potential drawbacks have been highlighted in the literature (e.g., material properties, specimen geometry, fixture geometry, through-the-thickness compression). The influence of friction was also studied, and authors provided controversial results ranging from a contribution of 2% (in the case of 4ENF) to 14% [31–34]. In addition to this, the use of test setups based on bending may be dramatically time-consuming in the case of fatigue testing due to the large displacements involved and low cycle frequency to be used [35] especially in the case of high cycle fatigue tests. Also, sample shifting up to 20 mm was observed in some case making necessary the implementation of new strategies [36]. Given the above, it seems clear that the existing methods are not readily amenable to the testing of hybrid interfaces, and it is worthy investigating a simpler setup.

These issues could be mitigated by characterising the mode II interfacial toughness using a more recently proposed test [37], the Transverse Crack Tension (TCT - also known as the Central Cut Plies test [38,39]), which has been modified and validated for monolithic unidirectional (UD) composites. Early results showed that the original TCT geometry does not allow for a pure mode II delamination to be achieved, compromising the energy release rate calculation. The specimen geometry was revised to include four symmetrical longitudinal pre-cracks emanating from the central transverse crack and was renamed as the modified Transverse Crack Tension (mTCT). This improved geometry delivered the desired results with good repeatability and reliability. Fatigue [32,35,40] and dynamic [41] loading scenarios were also investigated, with the results confirming the robustness of the mTCT method for characterising monolithic mode II interlaminar fracture.

To the authors' best knowledge, even though the original TCT geometry, with its aforementioned shortcomings, has already been used to characterise hybrid composites [17], the much-improved mTCT configuration was not yet explored. This work seeks to address this gap, by assessing the validity of the mTCT test for characterising the mode II fracture of fibre-metal hybrid interfaces. After presenting an appropriate analytical model for a hybrid mTCT test, a parametrical numerical analysis is conducted, investigating the influence of material and geometrical parameters on the test outcome. The numerical analysis outputs provided the design bounds for manufacturing hybrid fibre-metal test specimens. Experimental tests were performed to validate the proposed method, with the Digital Image Correlation (DIC) technique used to directly evaluate the full strain fields around the pre-crack tips. The experimental results were then fed to the analytical model to obtain the mode II fracture toughness. Results demonstrate that the mTCT configuration can successfully be extended to the case of hybrid composite for the assessment of the mode II fracture toughness of hybrid metal/composite interfaces.

2. Materials and Methods

2.1 Material and manufacturing process

Hybrid sandwich-like panels were fabricated using six plies of Hexcel (Stamford, United States of America) M79 UD600 prepreg composite [42] for the core (nominal cured ply thickness of 0.55 mm, total nominal core thickness of 3.3 mm), and $1.5mm$ thick CorTen steel plates (ASTM A606 HSLA Steel, Cold Rolled Sheet [43]) for the outer skins. The relevant mechanical properties of the two materials are reported in Table 1. A Hexcel HexBond™ 679 resin film [44] was used to adhere the metallic skins to the composite core. To prepare the metal substrates for the co-curing process, the substrates were roughened by using 100-grit sandpaper and opportunely degreased by using acetone. A hybrid 150x270 mm^2 panel was co-cured under vacuum at 70 ºC for 8 hours following the manufacturer's recommendations [42–44]. Once cured, samples with nominal dimensions of 250 x 15 mm^2 were machined using a waterjet cutter. It is important to point out that the unusual combination of steel and CFRPs in this context is not proposed as a technological solution. The samples were manufactured and tested with the aim of demonstrating that this configuration can be applied to hybrid interfaces in general. A different choice of material for the mechanical tests does not affect the validity of the results. Moreover, using stiffer materials as the outer layers could result in the central composite layer bearing a smaller portion of the load and the stress would likely follow the outer stiffer plates, potentially leading to metal plasticization before the crack onset. However, as this effect was considered in the sample design and plasticization monitored during the tests and simulated via FEM, it does not undermine the general conclusions drawn from the results of this study.

A schematic through-thickness representation of a hybrid mTCT sample is given in Figure 2(a), while the manufactured panel and a representative specimen are shown in Figure 2(b). In this figure, the position of the transverse crack is reported as a reference, in red, while the longitudinal pre-cracks departing from the transverse pre-crack are highlighted in Figure 2(a). While the transverse pre-crack is created by cutting the composite core reinforcement during the layup process, the longitudinal pre-cracks are manufactured through the insertion of a non-perforated polytetrafluoroethylene release film with a thickness of 13µm. The longitudinal pre-crack length $2a = 60mm$ was chosen according to the results of the parametrical numerical model presented in the following paragraphs.

Table 1 – Relevant Mechanical Material Properties

		Composite	**Metal**
Property	***Unit***	***M79 UD600*** *[42]*	***ASTM A606****[43]*
Ultimate Tensile Strength – σ_u	[MPa]	2120	≥ 448
Yield Strength – σ_y	[MPa]	$N.A.$	≥ 310

Tensile Modulus – E_{11}, E_m	[GPa]	137	205
Tensile Modulus – E_{22}	[GPa]	10.4	$N.A.$
Shear Modulus – G_{12}, G	[GPa]	5.4	80
Poisson Ratio – ν_{12}, ν	[ ]	0.25	0.28

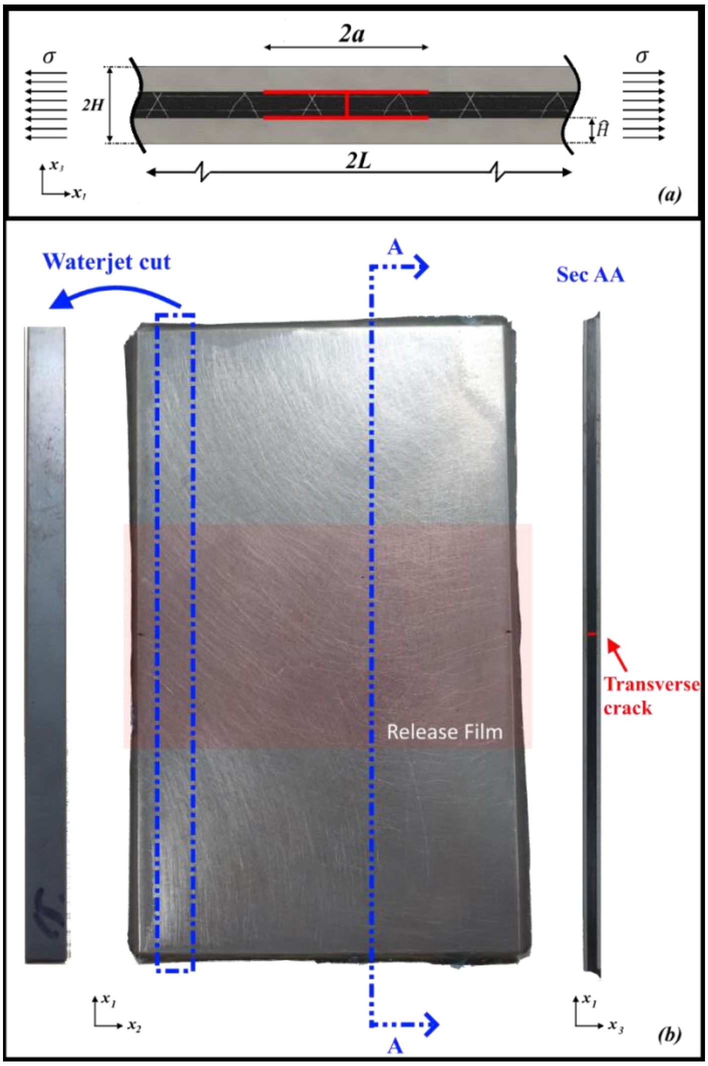

Figure 2 – (a) Through-thickness schematic view of a mTCT sample; (b) Hybrid panel, sample and cross-section (Sec AA)

From Figure 2(a), the following specimen parameters are defined:

- a- pre-crack half-length;
- $2H$ - total thickness;

- $2L$ - total length;
- $\hat{H}$ - single outer skin thickness;
- x_1 - principal direction (fibre direction);
- x_3 - through-thickness direction;
- σ – remote stress in the principal direction.

2.2 Digital Image Correlation and Quasistatic Tests

A 2D-DIC was carried out during the tests to evaluate the full strain field, focusing on the area around the longitudinal pre-crack tips. In the context of this study, DIC was used solely to directly observe the strain field, with a focus on the magnitude of ε_{33} as a key value to demonstrate that the mode I contribution can be neglected. To do so, images were captured at 0.3 Hz using a Single Lens Reflex Camera triggered remotely by the open-source software digiCamControl. Figure 3(a) shows the test setup. Due to the high degree of specimen symmetry, the acquisition of the images was limited to half the sample, so that a higher resultant resolution could be obtained around 1 set of pre-crack tips (Figure 3 (b)). More information on the hardware and DIC parameters is reported in Table 2.

Table 2 - Photomechanical setup

Parameter	**[-]**
Camera Type	Canon EOS 80D
Camera Resolution	24.2 MPixels
Image sensor size	CMOS 22.3 x 14.9 mm^2
Lens	Canon EF 100mm f/2.8L Macro IS USM
Sampling Rate	0.3 Hz
DIC - Subset Radius	30 Pixels

DIC – Subset spacing	6 Pixels
Strain radius (SR)	5 Grid nodes
Resultant Resolution	$16\,\mu m/pixel$

Quasi-static tensile tests were carried out using a servo-hydraulic universal testing machine MTS 810 (MTS Systems Corporation, USA) equipped with a 100 kN load cell. The cross-head speed was set to 1.5 mm/min and load-displacement curves were recorded. Samples were painted with a matte black-on-white speckle on one of the through-thickness surfaces for DIC purposes. DIC analysis and data post-processing was done using an open-source Matlab®-based plugin (i.e., Ncorr [45]).

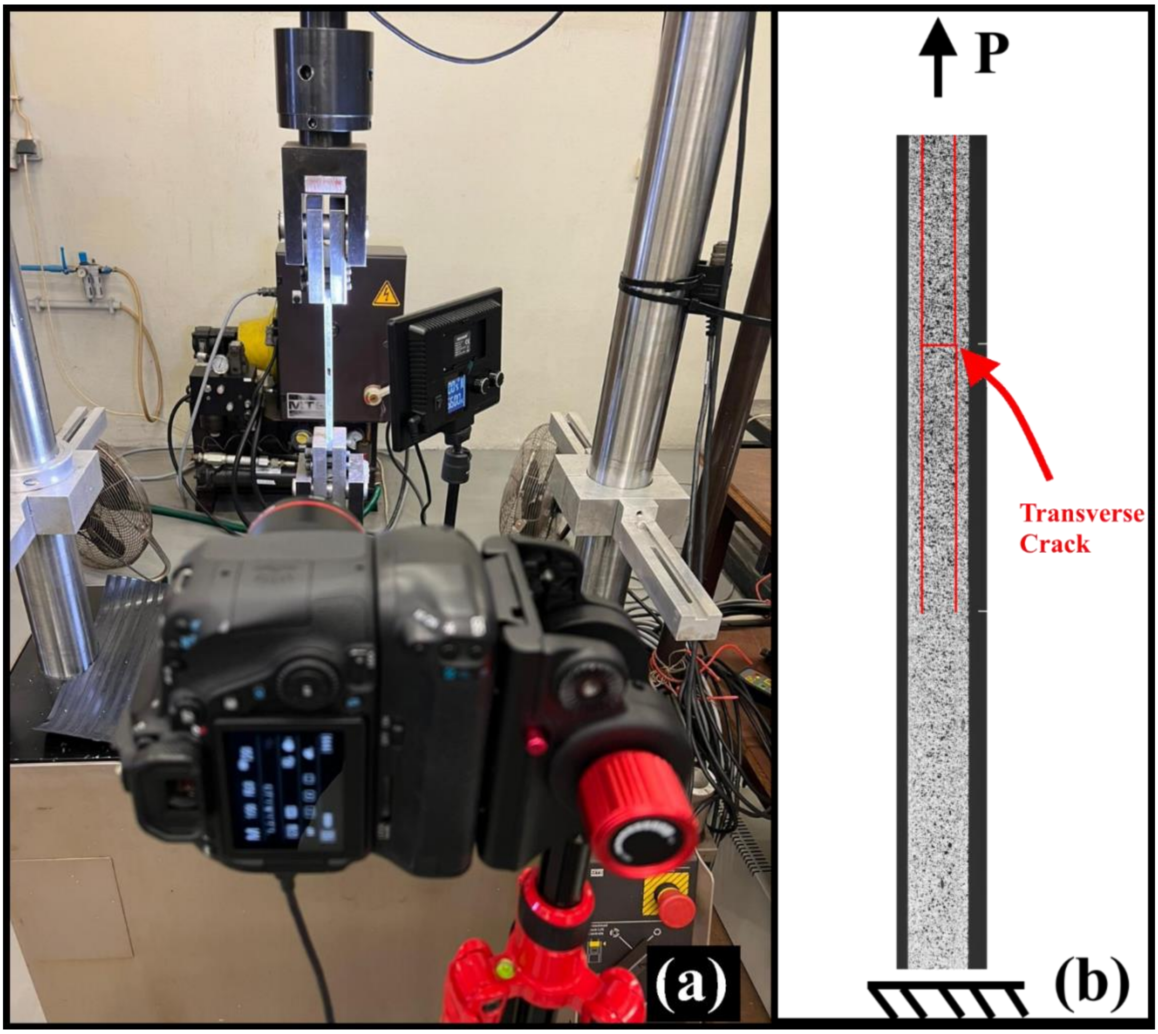

Figure 3 – (a) Test setup; (b) Sample picture acquisition for DIC analysis (loading setup schematized).

2.1 Analytical Model and FEM

As shown in previous works [37,40,46], the mode II energy release rate (ERR) for the case of monolithic composites can be calculated as [35,46]:

$$G_{II} = \sigma^2 \frac{H}{2E_{11}}\left(\frac{1}{1-\eta} - 1\right) \quad \textbf{Eq. 1}$$

where $\eta = 1 - \frac{\hat{H}}{H}$, with $\hat{H}$ and H as defined in the schematic of Figure 2(a).

However, in the case of hybrid composites, when materials of different natures are used in the stacking sequence, and the interface (i.e., where delaminations arise) is between layers with dissimilar properties, the mismatch between material characteristics must be factored into Eq. 1. In the case of isotropic metal substrates, the following Eq. 2 and Eq. 3 can be used for the determination of the mode II ERR[46]

$$G_{II} = \frac{1}{\Psi}(\sigma - \Delta T \Delta\alpha \eta E_m)^2 \quad \textbf{Eq. 2}$$

$$\Psi = \frac{2E_{11}[(1-\eta) - (1-k)\varphi\eta][1-(1-k)\varphi\eta]}{H\eta} \quad \textbf{Eq. 3}$$

where

$$\varphi = \frac{t}{H\eta}; \quad \textbf{Eq. 4}$$

$$\kappa = \frac{E_m}{E_{11}} \quad \textbf{Eq. 5}$$

and t is equal to the thickness of a single metal layer (N.B., t takes into account the possibility to limit the metal layer to a fraction of the thickness of the outer skin so that $t = \hat{H}$ if the outers skins are entirely made of metal – see Figure 4 (a)) , E_m is the Young's modulus of the metal, ΔT is the difference between the manufacturing process temperature and the testing environment temperature, and $\Delta\alpha$ is the difference between the coefficients of thermal expansion of the composite and metallic layers.

The second term within the parentheses of Eq. 2 accounts for the mismatching thermal expansions of the skin and core materials that result in manufacture-induced residual stresses at the interface. If the critical stress (i.e. the nominal remote stress at delamination, σ_d) is used in Eq. 1 or Eq. 2, the mode II interlaminar fracture toughness, G_{IIc}, can be obtained. It is worth noticing that both equations are independent of the crack length (provided there is a uniform stress distribution in the cracked region far from the crack tips – i.e., stresses are uniaxial in the ligaments) and material orthotropy. To include them in the analysis, an alternative formulation can be used in terms of stress intensity factor (SIF), as previously reported in [37], using an orthotropic rescaling technique [47,48]. The ERR can be expressed as:

$$G_{II} = \left(b_{11}b_{33}\frac{1+\rho}{2}\right)^{\frac{1}{2}}\lambda^{1/4}K_{II}^2 \qquad \textbf{Eq. 6}$$

where:

- $b_{ij} = s_{ij} - s_{i2}\, s_{j2}/s_{22}$;
- s_{ij} are the elements of the compliance matrix, S_{ij};
- $\lambda = b_{11}/b_{33}$;
- $\rho = \frac{2b_{13}+b_{55}}{2\sqrt{b_{11}b_{33}}}$;
- $K_{II} = \sigma\sqrt{H}\chi$ is the stress intensity factor;
- χ is the correction factor for geometry and material elasticity;
- $\alpha = \frac{a}{H}$, the crack length ratio.

In the case of using adhesives specifically designed to mitigate the effect of the mismatch between the coefficients of thermal expansion, or when using room or low-temperature curing resins, the contribution due to the thermal properties can be neglected. It is worth noting that, in the context of the present study, the adhesive and the prepregs used to manufacture the hybrid composites exhibits these characteristics. For hybrid composites, assuming that the specimen is significantly longer than the longitudinal pre-crack length, the correction function can be expressed as:

$$\chi = \chi(\alpha, \eta, \varphi, \lambda, \rho, \kappa, \tau) \qquad \textbf{Eq. 7}$$

with $\kappa = \frac{E_m}{E_{11}}$ and $\tau = \frac{E_m}{G_m}$, where G_m is the shear modulus of the metal.

The above formulation enables a parametrical numerical analysis to investigate the influence of the various geometrical and elastic parameters on the correction function, as well as the fracture mode-mixity, that is here defined as:

$$\psi = \frac{G_{II}}{G_I + G_{II}} \qquad \textbf{Eq. 8}$$

where $\psi = 0$ corresponds to a pure mode I opening, while $\psi = 1$ corresponds to pure mode II.

A 2D Finite Element model was prepared in Abaqus® [49]. Two different configurations were modelled as shown respectively in Figure 4(a) (i.e. thin metal layers interleaved in the stacking sequence) and Figure 4(b) (sandwich-like configuration with outer metal layers). For the sake of conciseness, this paper only presents the results for the specimen configuration of Figure 4(b) as those for Figure 4(a) were coherent and redundant. Similarly, we limit the presented results to the single case of $\eta = 0.5$, even if the discussion in the following section can be extended to other values of η. Due to the high degree of symmetry, only one quarter of the specimen geometry was modelled, imposing symmetry constraints. Four-node plane strain reduced-integration elements (CPE4R) were used for discretisation, and linear elastic simulations were performed (Figure 4(c)) [49]. The ERR was calculated at the crack tip via the Virtual Crack Closure Technique (VCCT) [50]. A python-based iteration file was used to run simulations for individual combinations of elastic and geometrical parameters, as per Eq. 7.

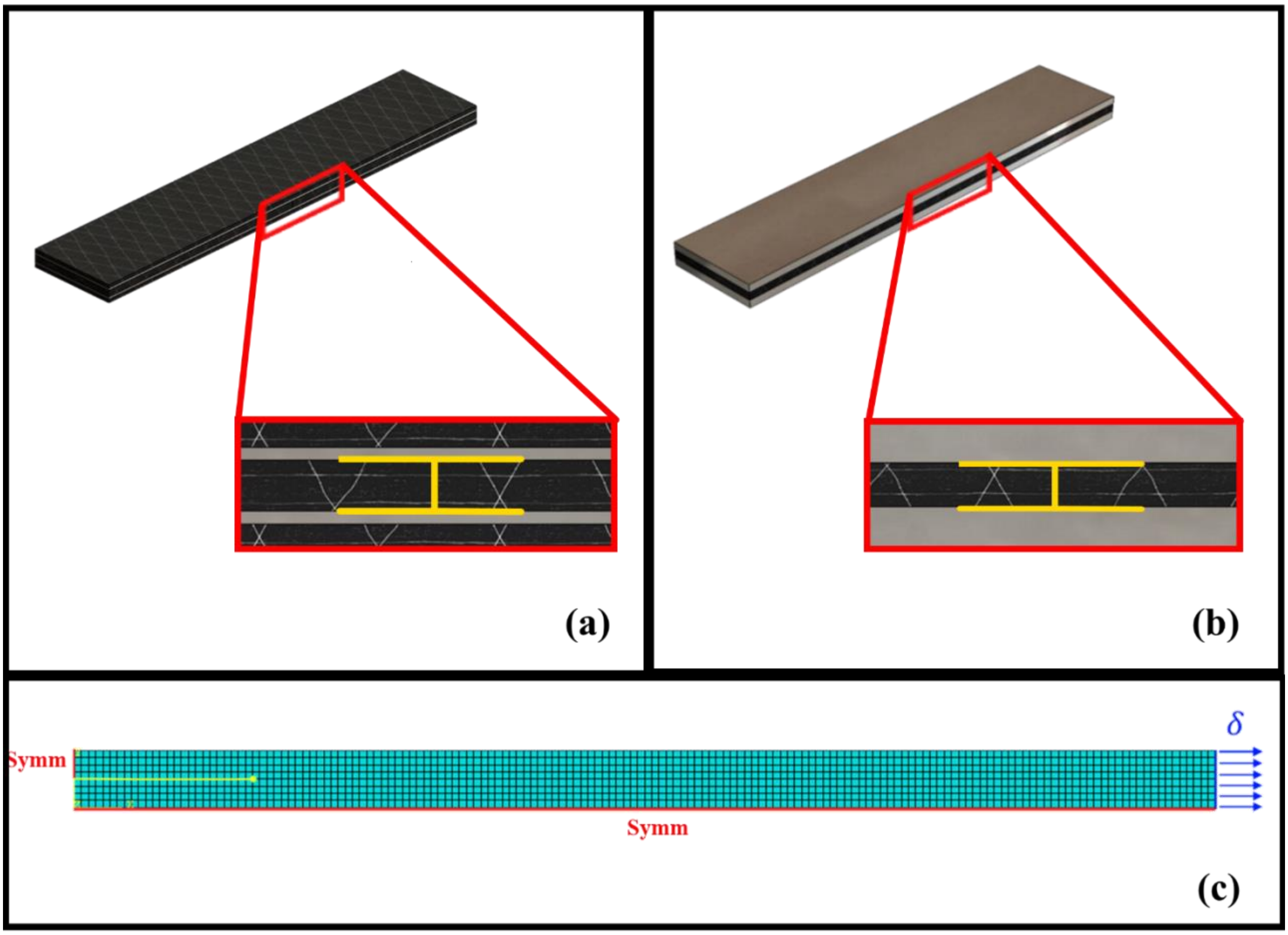

Figure 4 – Numerical models: (a) interleaved layup; (b) sandwich-like layup; (c) schematic representation of the 2D quarter-specimen model.

To further validate the hypothesis and demonstrate the general conclusions drawn in this study, a 3D finite element model of the hybrid mTCT sample was implemented in Abaqus Explicit. By exploiting the symmetry of the specimen, only one quarter of it was modeled to reduce computational costs. The two substrates were modeled using C3D8R elements with an approximate global mesh size of 0.5 mm, while the interface was modeled using a built-in cohesive contact behavior. Material and interface parameters are reported in Table 3. It is worth noting that the material parameters were taken from various sources, including manufacturers' datasheets and data obtained from experimental tests. For the contact parameters, conservative values were chosen based on data from literature. This choice was made under the assumption that a composite-composite interface is generally more efficient than a hybrid interface. Following this reasoning, the

Mode I and Mode III ERRs were chosen to represent a composite-composite interface for the normal and shear-2 stresses, while the shear-1 stress [49] was set equal to the interlaminar shear strength (ILSS) reported in the material datasheet [42]. It is important to highlight that, given the lack of experimental data related to the materials, the goal of running these simulations is not to reproduce the exact Force vs. Displacement experimental curves but to demonstrate the robustness of the configuration, which is independent of the combination of materials used to manufacture the samples.

Table 3 – Substrate and interface parameters used in the FE model.

Material	Parameter	Value	Unit	Source
Steel	Density	7.83	g/cm³	Material Datasheet [43]
	Young's Modulus E	201.4 (199.5 - 202.7)	GPa	In-house testing [51]
	Poisson's Ratio ν	0.28	-	Material Datasheet [43]
	Plastic Regime of the Stress vs. Strain curve	-	-	In-house testing [51] (the experimental curve of the steel is not reported for sake of conciseness).
	Yield Strength	330.0 (325.1 – 333.0)	MPa	In-house testing [51]
Composite	Density	1.75	g/cm³	Material Datasheet [42]
	Young's Modulus E_1	137000.0	MPa	
	Young's Modulus E_2	10400.0	MPa	
	Young's Modulus E_3	10400.0	MPa	
	Poisson's Ratio ν_{12}	0.25	-	
	Poisson's Ratio ν_{13}	0.25	-	
	Poisson's Ratio ν_{23}	0.3	-	
	Shear Modulus G_{12}	5400.0	MPa	
	Shear Modulus G_{13}	5400.0	MPa	
	Shear Modulus G_{23}	4000.0	MPa	
Interaction Properties	Normal Fracture Energy* [49]	0.28	N/mm	Estimated value [37]
	1st shear fracture energy** [49]	1.08	N/mm	From mTCT tests
	2nd shear fracture energy*** [49]	2.0	N/mm	Estimated value [37]
	Max normal stress [49]	40.0	MPa	Estimated value [37]
	Shear-1 [49]	56.0	MPa	Estimated value [42]
	Shear-2	20.0	MPa	Estimated value [37]

*Nominal stress at damage initiation in a normal-only mode.

**Nominal stress at damage initiation in a shear-only mode that involves separation only along the first shear direction.

***Nominal stress at damage initiation in a shear-only mode that involves separation only along the second shear direction.

3. Results and Discussion

This section first presents the results of the numerical parametrical analysis, from which the specimen geometry used in the experimental campaign was decided. Experimental test results are then presented to validate the proposed methodology.

3.1 Parametrical analysis

Figure 5 and Figure 6 respectively present the relevant mode-mixity, ψ, and correction factor, χ, results of the parametrical study for different elastic material parameters, including the orthotropy of the composite core (i.e. different combinations of λ and ρ) and the metal-to-composite elastic stiffness ratio, κ (see Eq. 5).

For sake of conciseness, Figure 5 reports the results related to $\kappa = 1.5$, $\lambda = 0.01$ and $\rho = 1.0$ as it was observed that κ does affect ψ significantly and the results for different values are redundant and coherent. In other words, it can be stated that the mode-mixity results can be considered valid whatever the combination of composite system and metal layer (i.e., the elastic properties of the metal and composites used to perform the test do not affect the robustness of the results). However, this same figure highlights a clear dependence on the crack length ratio, α. Indeed, for very small crack lengths ($\alpha \rightarrow 0$), the mode I contribution cannot be neglected, and the analysis demonstrates that a pre-crack of sufficient length ($\alpha > 0.5$) should be introduced in the specimens to obtain a pure mode II. This result agrees with what was previously reported for monolithic composites [37].

Moreover, Figure 6a, b and c report the variation in $\chi(\alpha)$ by keeping some of the parameters fixed, to appreciate their influence on the correction function and gives further insight into the behaviour of the proposed geometry, providing a more stringent lower bound to the pre-crack length ratio design. In fact, it can be noticed that χ is non-linearly dependent on α up to a value of almost $\alpha = 3$. Thus, a longitudinal pre-crack length ratio lower than 3 would require the crack length to be measured before being able to obtain a correct determination of the mode II ERR. On the other hand, if $\alpha \geq 3$, the value of χ stabilises, rendering it independent of the crack length ratio, and the analytical formulae presented in Eq. 2 to Eq. 5 can be used in the calculation of the ERR, taking the first delamination load to determine the critical propagation stress, σ_d. According to these results, $\alpha_t = 3$ can thus be considered as a threshold value in the design of experimental coupon geometries. This conclusion can be extended to all the combinations of ρ, λ and κ analysed in this study and results are not here shown for seek of clineariness. Considering the stability of χ and ψ for $\alpha \geq 3$, the parametric study proceeded to investigate the variation in the steady-state value of χ as a function of the elastic parameters λ, ρ, κ and τ. Polynomial surface functions were fit to the numerically derived χ values. Figure 7 presents the results of this study for fixed sets of values of τ and κ. Figure 7(a) shows a clear influence of κ on χ, and this effect is amplified for low values of ρ. On the other hand, as shown in Figure 7(b), the influence of τ is not as strong, and can be reasonably neglected, so that the dependency of χ on this parameter can be eliminated. Finally, Figure 7(c) reports a singular representative surface for $\kappa = 1.5$ and $\tau = 2.5$, roughly equating to the elastic parameters for the composite and metallic materials (refer to Table 1) to be used experimentally.

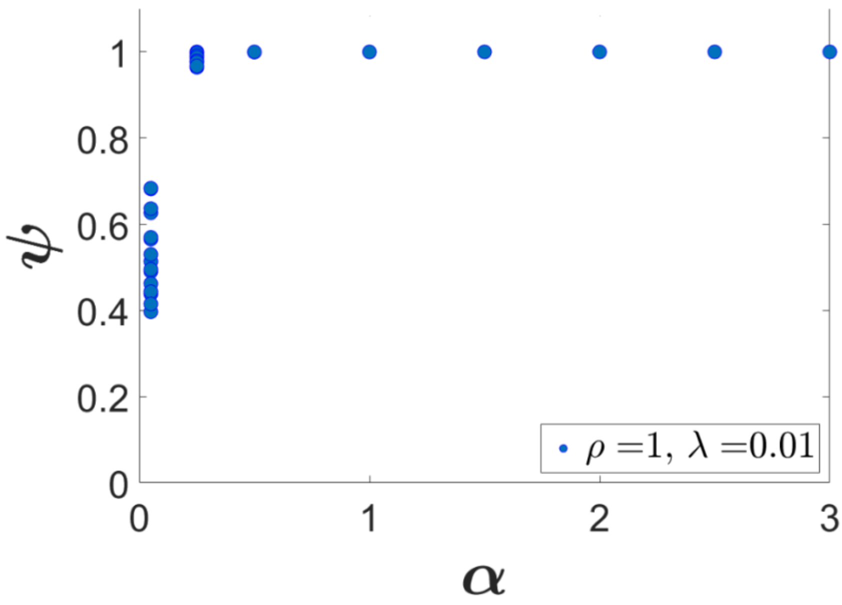

Figure 5 – Variation of the mode-mixity, ψ, for elastic parameter ratios of: $\kappa = 1.50$.

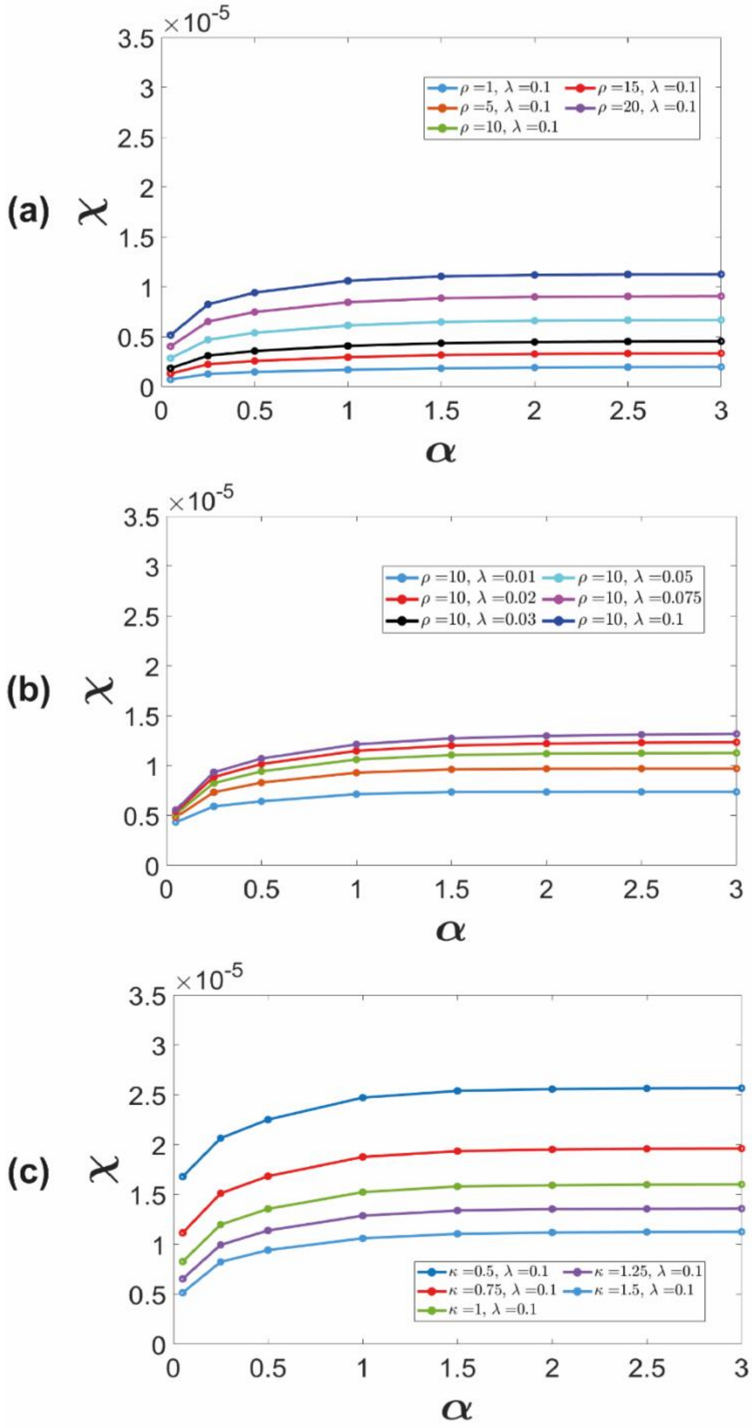

Figure 6 – Variation of the correction function, χ, for elastic parameter ratios of (a) $\kappa = 1.5, \rho = 10.0$; (b) $\kappa = 1.5, \lambda = 0.1$; (c) $\rho = 10.0, \lambda = 0.1$.

Employing a polynomial function of the form:

$$\chi = \sum P_{ij} \lambda^{i-1} \rho^{j-1} \qquad \textbf{Eq. 9}$$

the matrix of coefficients corresponding to the fitted surface presented in Figure 7(c) is:

$$P = \begin{bmatrix} 0.132 & 0.022 & -0.010 & 0.003 \\ -0.032 & -0.006 & 0.002 & 0 \\ 0.014 & 0.003 & 0 & 0 \\ 0 & 0 & 0 & 0 \end{bmatrix} \qquad \textbf{Eq. 10}$$

With a coefficient of determination $R^2 = 0.9839$.

Based on the results just presented, the experimental specimen geometry was subsequently designed (dimensions reported in section 2.1), manufactured, and tested. The results of the experimental campaign are reported in the next section.

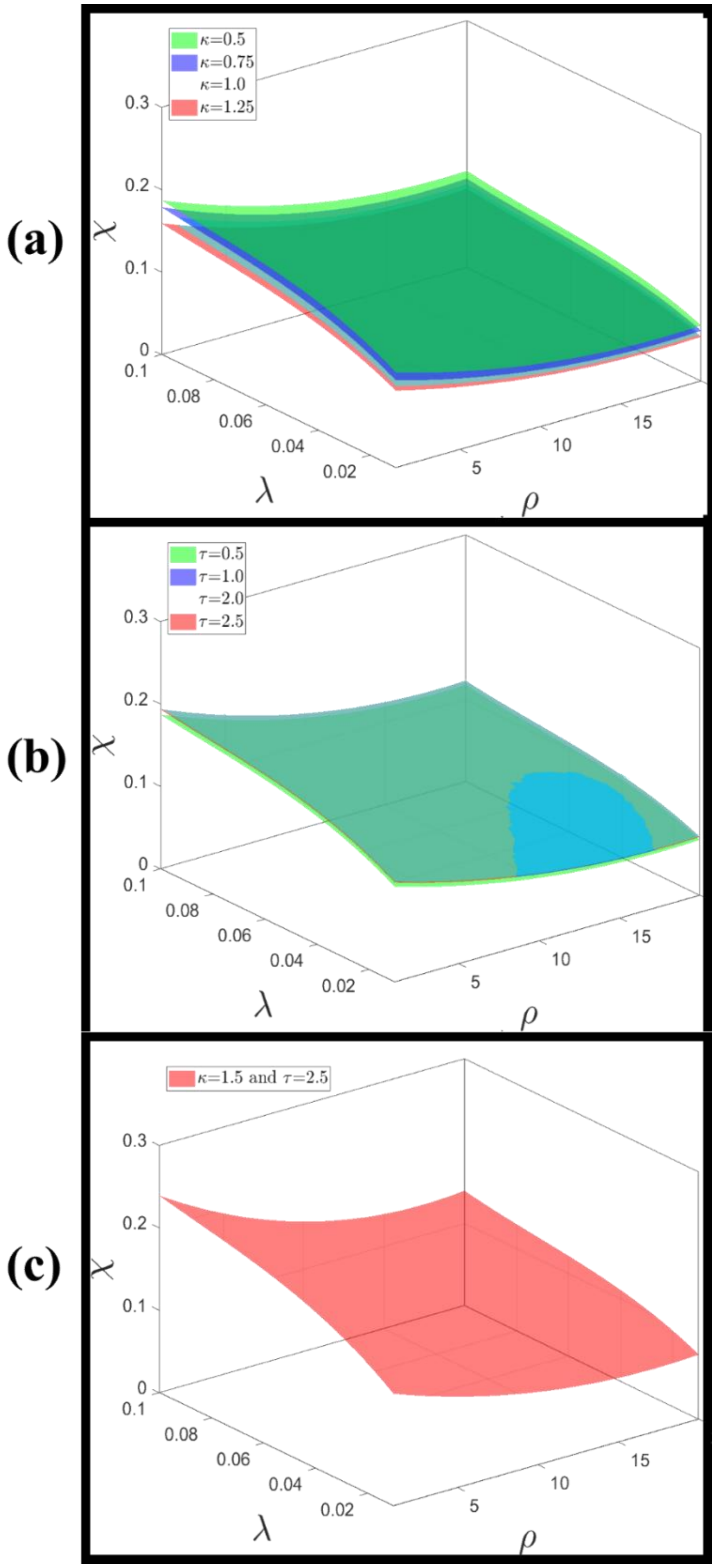

Figure 7 – Steady-state values of $\chi(\lambda, \rho)$ for: (a) $\tau = 1.0$; (b) $\kappa = 1.0$; (c) $\kappa = 1.5 \wedge \tau = 2.5$

3.2 Experimental campaign and Numerical Validation

Five samples were tested using the experimental setup presented in section 2.1. DIC was employed on three samples for redundancy. Figure 8 reports a typical load vs. displacement curve obtained for one of the tested hybrid mTCT specimens. It is worth noting that this kind of curve possesses characteristics that are representative of both fully metallic and monolithic composite mTCT specimen tests [37]. In particular, point (A) (~12500 N) corresponds to the failure of the resin pocket that forms at the transverse crack during manufacturing, due to the resin bleeding between the two composite core halves. This point is followed by the steel yielding (between points (B) and (C) - ~14000N) and hardening, until the onset of mode II longitudinal crack propagation, occurring at point (D) (~17500N). However, the change in slope in the load-displacement curve is subtle, as is commonly observed for TCT specimens [37]. In this work, DIC was used to confirm the onset of cracking. In this regard, the mTCT specimen, which incorporates a pre-crack, offers more consistent and predictable crack propagation compared to the TCT specimen. In the latter, cracks tend to initiate in resin pockets near the cut, potentially resulting in less uniform propagation. From this perspective, the mTCT specimen demonstrates superior performance. Post-test examination of the fracture surfaces revealed no indications of non-self-similar crack propagation. The propagation of the longitudinal cracks is registered up to point (E), and the load in this region is plateaued. Once these cracks reach the region of the specimen which is compressed by the machine grips, the apparent fracture toughness rises, and the propagation stops. From this point, the contribution of the composite substrates can be neglected, and the metal substrates proceed to harden further. The test was stopped before the metal skin layers could fail, since this stage is of no value to the data reduction carried out in this work.

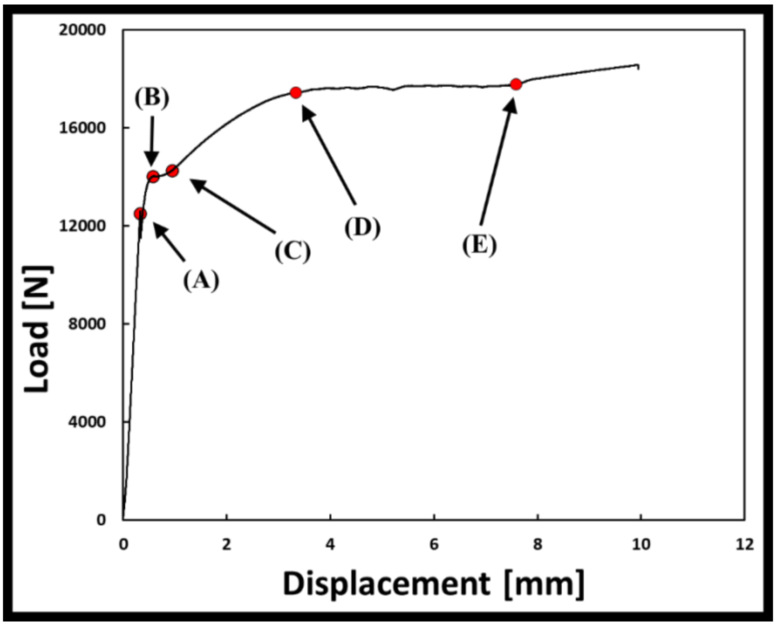

Figure 8 – Typical load vs. displacement curve of a hybrid mTCT specimen.

As mentioned before, delamination propagation occurs when the metallic skins are already undergoing plasticity. As reported by Fink et al. [46], Eq. 2 and Eq. 3 are only valid in the elastic regime. This condition could be particularly restrictive for a classic TCT geometry, where the longitudinal crack tips at the edges of the transverse crack find themselves in the metallic region subjected to the maximum stress, undergoing plasticity. In the case of an mTCT, the artificial longitudinal pre-cracks ensure that the crack tips are located far from the central region, in an area where stress levels decrease due to the geometric variation of the cross-section. Thus, it is reasonable to assume that an elastic regime area surrounds the pre-crack tips, and that the formulae of Eq. 2 and Eq. 3 are still valid, so that the delamination propagation load (i.e. point (D)) can be used for the calculation of the critical ERR. This is also confirmed by Figure 9 where the DIC was locally applied to highlight the above describe scenario just prior the crack propagation. It is worth noting that the strain level is above the yield strain in the ligament area while a gradient exists across the crack tip zone with strains. Moreover, this hypothesis is confirmed by the results from the numerical validation presented in the following paragraph.

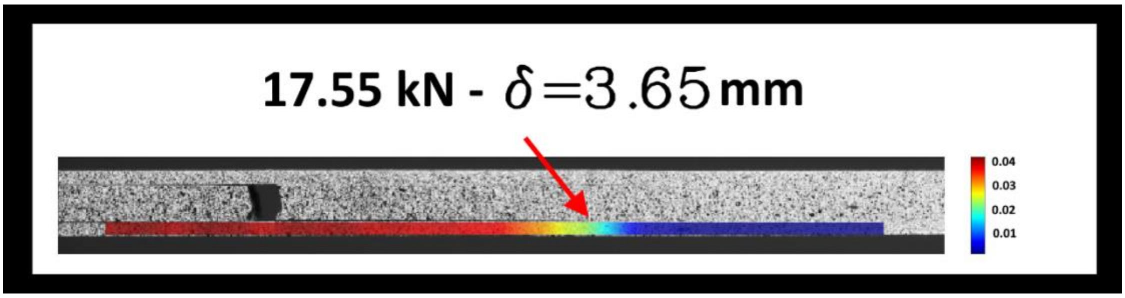

Figure 9 - DIC analysis on th the metal substrates - ε_{11} – Cracktip highilighted by the red arrow

The experimental test results, and the subsequently calculated values for steady-state mode II fracture toughness, are reported in Table 4.

Table 4 – Results from the experimental tests

	L_d *[N]*	σ_d *[MPa]*	G_{IIc} *[N/mm]*
Average	17547	170.8	1.08
Standard Dev. [%]	0.62%	0.62%	0.85%
95% CI	[17460; 17634]	[169.9; 17.6]	[1.08; 1.09]

Figure 10 reports a sequence of contour plots for through-thickness deformation, ε_{33}, obtained from DIC analysis. The other strain components are of no significant interest to this work and are thus not presented. The region of interest for DIC analysis was limited to the area right ahead of the transverse crack, to mitigate the noise deriving from high-correlation-factor calculations, due to the discontinuity arising from the breakage of the resin pocket and the consequential disruption of the painted speckle layer in that zone. This strategy allows for better focusing on the pre-crack tips. The image corresponding to 12.5 kN was taken right before the resin pocket breaks (Figure 8, point (A)) while that at 14.2 kN was taken during the metal yield phase (Figure 8, point (B)). Due to the low level of load, the pre-cracks are not very visible, and the strain levels are close to zero. For a load equal to 17.3 kN, prior to the onset of delamination propagation (Figure 8, point (D)), the two pre-cracks are more noticeable. In this image, the high level of strains (in red) can be considered an artefact of the technique due to the discontinuity deriving from the speckle paint failure along the crack lines.

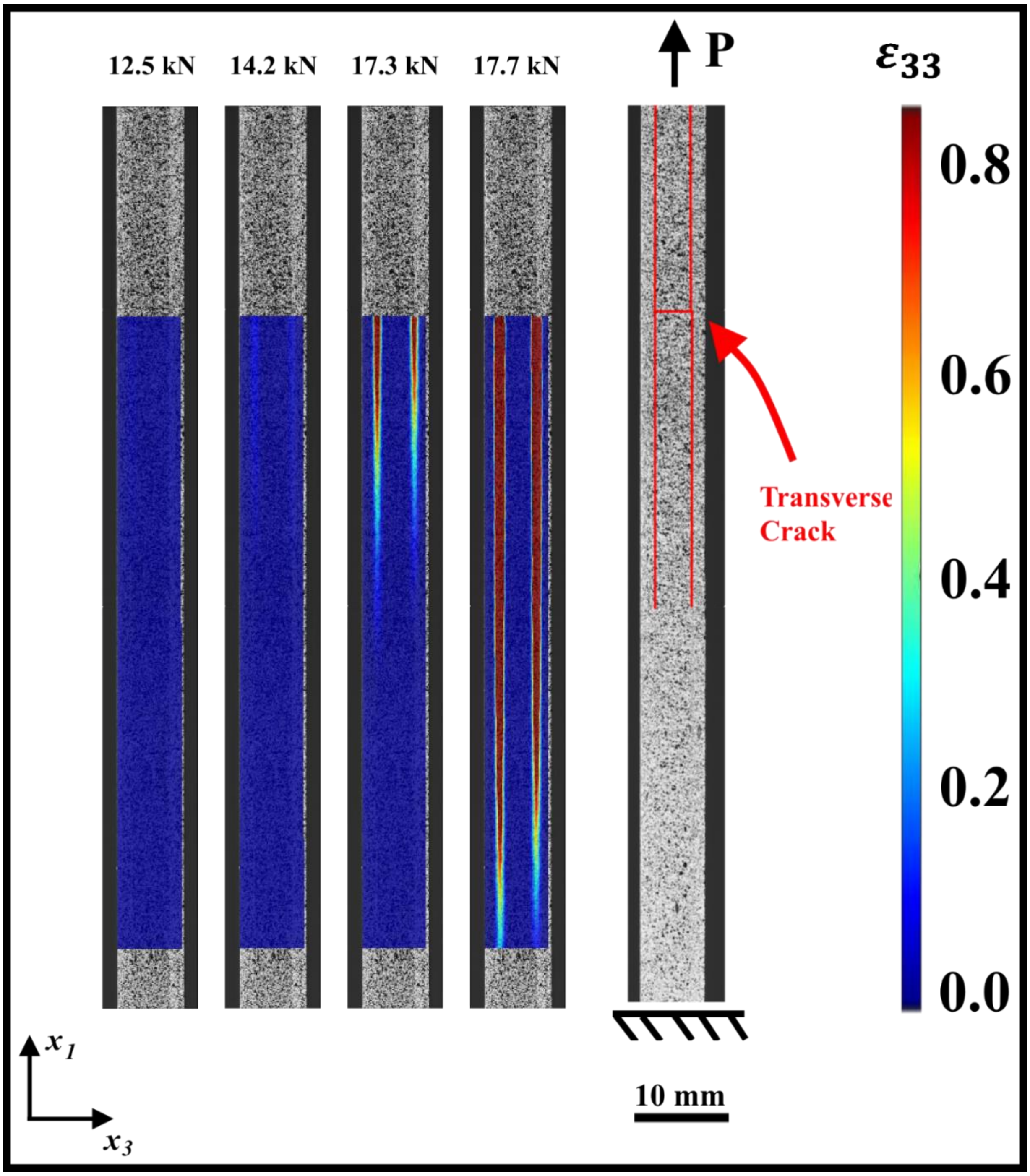

Figure 10 – Half-specimen DIC analysis results for through-thickness strains, ε_{33}.

On the other hand, the area surrounding the crack tips is characterised by a negligible amount of strain. If $\varepsilon_{33} \approx 0$, it can be concluded that the opening stress σ_{33} is also negligible. Given this reasonable assumption, the direct observation of the results of the full-field strain analysis confirms that the proposed test setup allows the hybrid interface fracture to propagate in pure mode II.

Furthermore, the slight asymmetry of the cracks that can be noticed in Figure 10 does not affect the robustness of the test and could be a result of a slight defect introduced during manufacturing (e.g., non-symmetric placement or mid-cure sliding of the two release films that form the pre-cracks).

For the sake of completeness, Figure 10 presents a final image corresponding to a point after full crack propagation (i.e., $P = 17.7kN$) and Figure 11 reports a DIC closeup analysis showing that $\varepsilon_{33} \approx 0$ in the area around the cracktip.

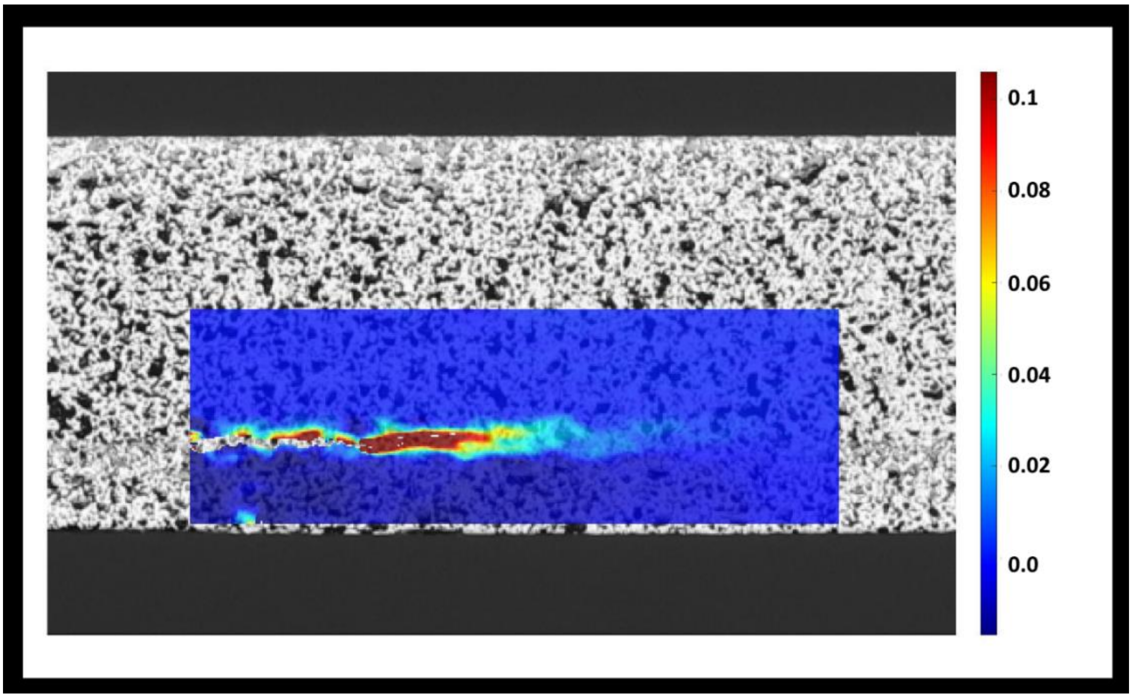

Figure 11 – DIC analysis of the area around the cracktip - ε_{33} – 17.55 kN

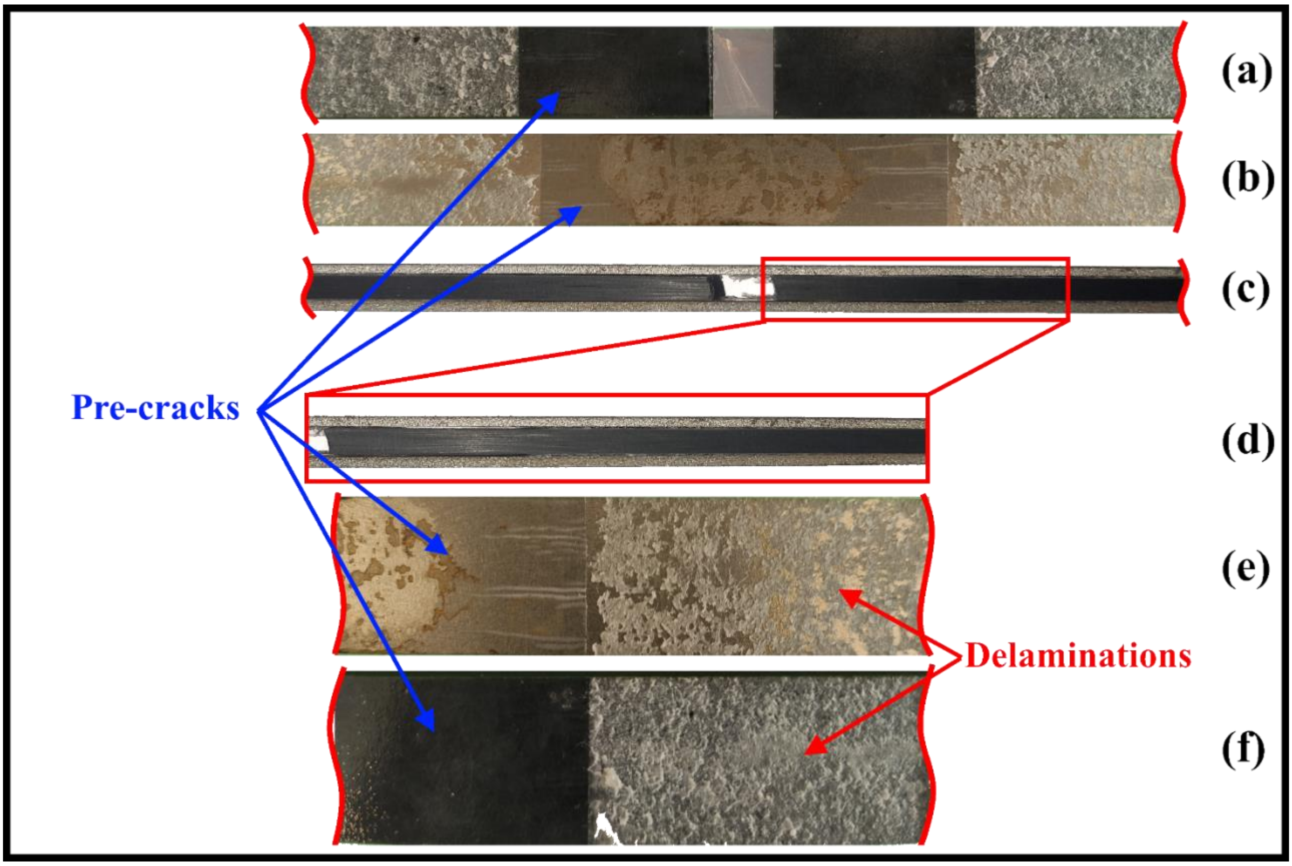

Figure 12 – Post-mortem fracture analysis: (a) delaminated surface – composite side; (b) delaminated surface – metal side; (c) side view; (d) side view – closeup; (e) delaminated surface closeup– composite side; (f) delaminated surface closeup– metal side;

The post-mortem fractured surfaces of one typical specimen are shown in Figure 12. In particular, in Figure 12 (a) and Figure 12 (b), the glossy smooth surface left by the release film is well visible and the pre-crack tips can be easily detected. Moreover, the plastic deformation can be observed in Figure 12 (c), from the permanent significant gap created between the core halves. From the closeup images (Figure 12 (d) to Figure 12 (f)), a mixed adhesive-cohesive failure mode can be observed. The fracture seems to be concentrated near the metal substrate, indicating that the adhesion could be further enhanced (e.g., through a surface chemical treatment). However, the enhancement of metal-adhesive compatibility is not being assessed in this work.

In Figure 13, the results from the 3D FEM simulation are presented. Specifically, the first non-zero value of the cohesive surface damage index helps to identify the crack onset. For this condition, the von Mises stresses are also shown, with a maximum value of 275.2 MPa, which is well below the steel yield strength at every point of the sample, including the crack tip.

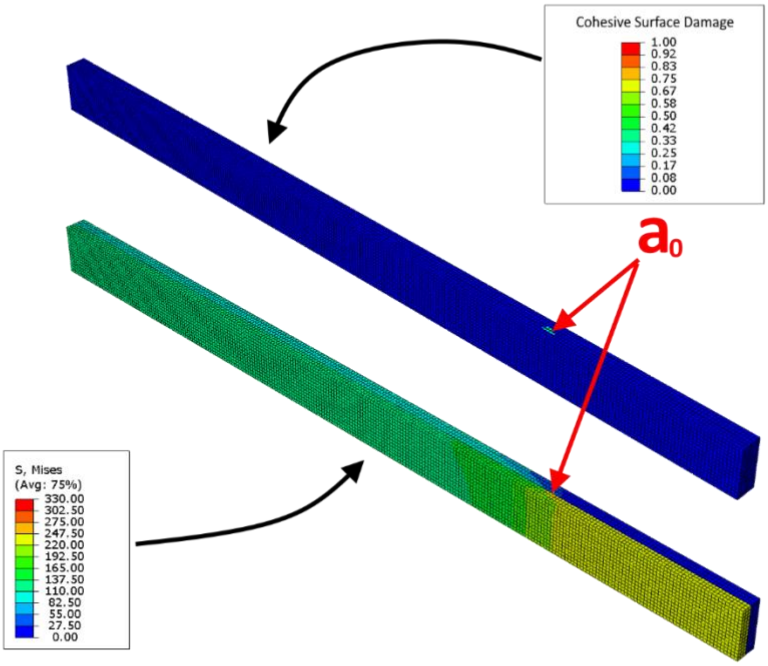

Figure 13 - Finite element model results: crack onset conditions

For higher loads, when propagation occurs, as mentioned earlier, the steel ligament may undergo plastic deformation. Figure 14 was generated under the condition in which the cohesive surface damage index reaches 1.0 for the first time at least at one point. In other words, this occurs when full propagation takes place, and the elements are fully damaged. Under this condition, the crack tip a' slightly migrated from its original position at a_0, the location of the artificial crack. If the von Mises stresses are plotted by applying a lower bound equal to the yield strength in the contour plot, it is possible to visualize the portion of the metal that has entered a plastic regime. From the same figure, it can be observed that the position of a' is in an area that remains within an elastic field. This further confirms that an elastic regime surrounds the pre-crack tips, that the Eq. 11 and Eq. 12 are still valid, and that the delamination propagation load can be used for the calculation of the critical ERR.

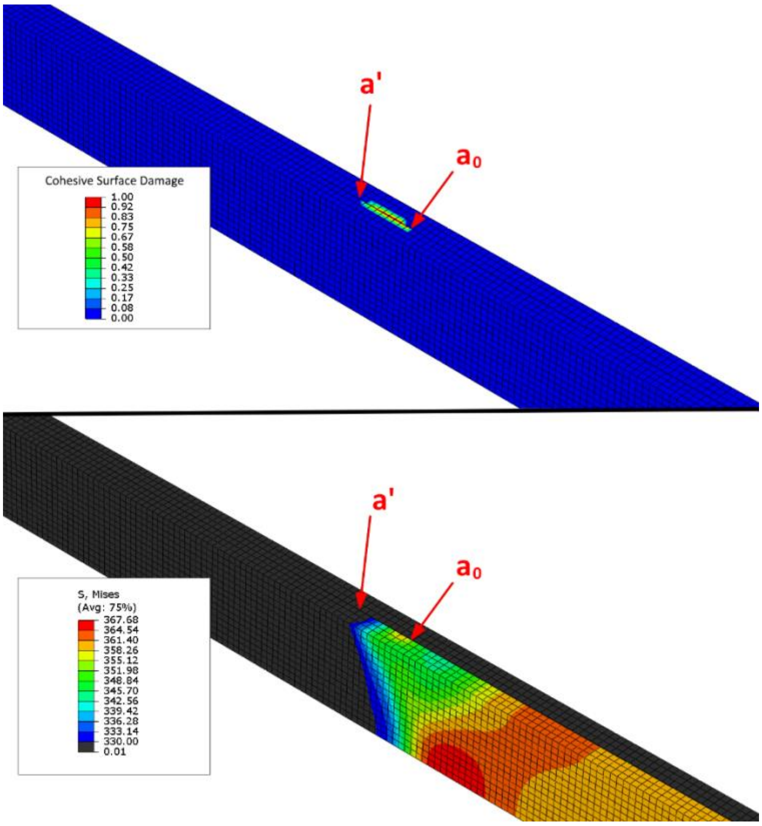

Figure 14 - Finite element model results: crack propagation conditions. Closeup.

Conclusions

In this work, the authors propose and investigate the possibility to extend the mTCT test methodology to the case of a hybrid interface (namely, a metal-composite), for the determination of the steady-state mode II interlaminar fracture toughness. The main results and final remarks can be summarised as follows:

- A parametrical numerical analysis was performed to investigate the suitability of the mTCT geometry for assessing the mode II fracture toughness of hybrid interfaces. In this framework, the influence of the geometrical and elastic material parameters was evaluated. Results showed that a classic TCT geometry (i.e. with no longitudinal pre-cracks, $a = 0$) would prevent the development of a pure mode II fracture, and thus it cannot be taken into consideration for the characterisation of the steady-state mode II fracture toughness. On the other hand, introducing two artificial pre-cracks (mTCT) allows a pure mode II condition to be achieved. Moreover, the numerical analysis provided the design parameters (i.e., lower-bound for the crack length ratio) used during the subsequent experimental campaign.

- The correction factor was only presented for particular combinations of material and geometrical parameters. However, the methodology can be easily extended to a wide range of material combinations.

- Introducing artificial pre-cracks provides additional advantages and widens the spectrum of possible metallic materials that can be used as substrates. In particular, assuming that the plastic region is reasonably limited to the middle portion of the specimen around the transverse crack, the pre-cracks shift the crack-tips to an elastic region, enabling the use of the elastic-based formulae for the calculation of the mode II fracture toughness. In itself, this enhances the robustness of the test method.

- The mTCT geometry was experimentally validated for hybrid interfaces for the first time. The DIC technique was successfully employed, enabling the evaluation of the through-thickness strains that allowed us to reach the desired conclusion, i.e. that the crack-tips are subjected to a pure mode II scenario before and during propagation. Moreover, the 3D finite elements model confirmed that the elastic regime conditions at the crack tips allow to use the classical equations for the calculation of the mode II ERR.

- The experimental campaign results showed very low levels of scatter, further demonstrating the robustness of the proposed test method.

- The proposed methodology provides the scientific community with a new test method for the determination of hybrid interface steady-state mode II fracture toughness. While the model has been validated for the metal/composite interface, it applies to a broad range of hybrid interfaces. The methodology may require further testing for other material combinations to ensure its transferability.

CRediT authorship contribution statement

T. Scalici: Conceptualization, Methodology, Software, Validation, Formal analysis, Investigation, Data curation, Writing – original draft, Writing – review & editing, Visualization. **D. Dalli**: Validation, Formal analysis, Investigation, Writing – original draft, Writing – review & editing, Visualization. **Z. Ullah**: Resources, Administration, Funding acquisition, Supervision, Writing – review & editing. **G. Catalanotti**: Conceptualization, Methodology, Software, Writing – review & editing, Supervision, Funding acquisition.

Declaration of Competing Interest

The authors declare that they have no known competing financial interests or personal relationships that could have appeared to influence the work reported in this paper.

Data availability

Data will be made available on request.

References

[1] McLaren Technology Group. Case study: Carbon Fibre 2016:2021. http://www.mclaren.com/technologygroup/case-studies/case-study-carbon-fibre/ (accessed November 4, 2022).

[2] Marsh G. Airbus A350 XWB update. Reinforced Plastics 2010;54:20–4. https://doi.org/10.1016/S0034-3617(10)70212-5.

[3] Aymen L. Aviation Knowledge-Aerodynamics-Meteorology. n.d.

[4] Carlsson LA, Donald •, Adams F, Pipes • R Byron. Experimental Characterization of Advanced Composite Materials. Experimental Characterization of Advanced Composite Materials 2014. https://doi.org/10.1201/B16618.

[5] Moore David, Pavan A., Williams JG. Fracture mechanics testing methods for polymers, adhesives, and composites. Amsterdam: Elsevier; 2001.

[6] Ramaswamy K, O'Higgins RM, Corbett MC, McCarthy MA, McCarthy CT. Quasi-static and dynamic performance of novel interlocked hybrid metal-composite joints. Compos Struct 2020;253:112769. https://doi.org/10.1016/J.COMPSTRUCT.2020.112769.

[7] Godwin EW, Matthews FL. A review of the strength of joints in fibre-reinforced plastics: Part 1. Mechanically fastened joints. Composites 1980;11:155–60. https://doi.org/10.1016/0010-4361(80)90008-7.

[8] Thoppul SD, Finegan J, Gibson RF. Mechanics of mechanically fastened joints in polymer–matrix composite structures – A review. Compos Sci Technol 2009;69:301–29. https://doi.org/10.1016/J.COMPSCITECH.2008.09.037.

[9] Pramanik A, Basak AK, Dong Y, Sarker PK, Uddin MS, Littlefair G, et al. Joining of carbon fibre reinforced polymer (CFRP) composites and aluminium alloys – A review. Compos Part A Appl Sci Manuf 2017;101:1–29. https://doi.org/10.1016/J.COMPOSITESA.2017.06.007.

[10] Nagarajan BM, Manoharan M. Assessment of dissimilar joining between metal and polymer hybrid structure with different joining processes. Journal of Thermoplastic Composite Materials 2021;36:2169–211. https://doi.org/10.1177/08927057211048534.

[11] Camanho PP, Tavares CML, De Oliveira R, Marques AT, Ferreira AJM. Increasing the efficiency of composite single-shear lap joints using bonded inserts. Compos B Eng 2005;36:372–83. https://doi.org/10.1016/J.COMPOSITESB.2005.01.007.

[12] Li R, Kelly D, Crosky A. Strength improvement by fibre steering around a pin loaded hole. Compos Struct 2002;57:377–83. https://doi.org/10.1016/S0263-8223(02)00105-8.

[13] Li R, Kelly D, Crosky A, Schoen H, Smollich L. Improving the efficiency of fiber steered composite joints using load path trajectories. J Compos Mater 2006;40:1645–58. https://doi.org/10.1177/0021998306060168.

[14] Hart-Smith LG. Adhesively bonded joints for fibrous composite structures . In: Tong L, Soutis C, editors. Recent Advances in Structural Joints and Repairs for Composite Materials, Dordrecht: Springer; 2003, p. 173–210.

[15] Fink A, Kolesnikov B. Hybrid titanium composite material improving composite structure coupling. European Space Agency, (Special Publication) ESA SP 2005:843–8.

[16] Herrera-Franco PJ, Cloud GL. Strain-Relief Inserts for Composite Fasteners -An Experimental Study. J Compos Mater 1992;26:751–68. https://doi.org/10.1177/002199839202600506.

[17] Fink A, Camanho PP, Andrés JM, Pfeiffer F, Obst A. Hybrid titanium-CFRP laminates for high-performance bolted joints. Compos Part A Appl Sci Manuf 2009;40:1826–37. https://doi.org/10.1016/j.compositesa.2009.02.010.

[18] Catalanotti G, Furtado C, Scalici T, Pitarresi G, van der Meer FP, Camanho PP. The effect of through-thickness compressive stress on mode II interlaminar fracture toughness. Compos Struct 2017;182:153–63. https://doi.org/10.1016/j.compstruct.2017.09.014.

[19] Cartié D, Davies P, Peleau M, Partridge IK. The influence of hydrostatic pressure on the interlaminar fracture toughness of carbon/epoxy composites. Compos B Eng 2006;37:292–300. https://doi.org/10.1016/j.compositesb.2005.12.002.

[20] Bing Q, Sun CT. Effect of compressive transverse normal stress on mode II fracture toughness in polymeric composites. Int J Fract 2007;145:89–97. https://doi.org/10.1007/s10704-007-9103-4.

[21] Yao Y, Shi P, Chen M, Chen G, Gao C, Boisse P, et al. Experimental and numerical study on Mode I and Mode II interfacial fracture toughness of co-cured steel-CFRP hybrid composites. Int J Adhes Adhes 2022;112:103030. https://doi.org/10.1016/j.ijadhadh.2021.103030.

[22] Ulus H, Kaybal HB, Cacık F, Eskizeybek V, Avcı A. Fracture and dynamic mechanical analysis of seawater aged aluminum-BFRP hybrid adhesive joints. Eng Fract Mech 2022;268:108507. https://doi.org/10.1016/j.engfracmech.2022.108507.

[23] ASTM. D7905/7905M - 14 - Standard Test Method for Determination of the Mode II Interlaminar Fracture Toughness of Unidirectional Fiber-Reinforced Polymer Matrix Composites 2014.

[24] Pérez-Galmés M, Renart J, Sarrado C, Brunner AJ, Rodríguez-Bellido A. Towards a consensus on mode II adhesive fracture testing: Experimental study. Theoretical and Applied Fracture Mechanics 2018;98:210–9. https://doi.org/10.1016/J.TAFMEC.2018.09.014.

[25] Abdel Monsef S, Ortega A, Turon A, Maimí P, Renart J. An efficient method to extract a mode I cohesive law for bonded joints using the double cantilever beam test. Compos B Eng 2019;178:107424. https://doi.org/10.1016/J.COMPOSITESB.2019.107424.

[26] International Organization for Standardization. ISO 15114:2014 - Fibre-reinforced plastic composites – Determination of the mode II fracture resistance for unidirectionally reinforced materials using the calibrated end-loaded split (C-ELS) test and an effective crack length approach 2014.

[27] Liu Q, Qiao P. Mixed mode fracture characterization of GFRP-concrete bonded interface using four-point asymmetric end-notched flexure test. Theoretical and Applied Fracture Mechanics 2017;92:155–66. https://doi.org/10.1016/J.TAFMEC.2017.06.009.

[28] Tsokanas P, Loutas T. Hygrothermal effect on the strain energy release rates and mode mixity of asymmetric delaminations in generally layered beams. Eng Fract Mech 2019;214:390–409. https://doi.org/10.1016/J.ENGFRACMECH.2019.03.006.

[29] Hwang SFA, Huang CC. Sliding mode interlaminar fracture toughness of interply hybrid composite materials. Polym Compos 1998;19:514–26. https://doi.org/10.1002/pc.10126.

[30] Mujika F, Tsokanas P, Arrese A, Valvo PS, da Silva LFM. Mode decoupling in interlaminar fracture toughness tests on bimaterial specimens. Eng Fract Mech 2023;290. https://doi.org/10.1016/j.engfracmech.2023.109454.

[31] Davidson BD, Sun X. Effects of friction, geometry, and fixture compliance on the perceived toughness from three-and four-point bend end-notched flexure tests. Journal of Reinforced Plastics and Composites 2005;24:1611–28. https://doi.org/10.1177/0731684405050402.

[32] Pitarresi G, Scalici T, Dellaira M, Catalanotti G. A methodology for the rapid characterization of Mode II delamination fatigue threshold in FRP composites. Eng Fract Mech 2019;220. https://doi.org/10.1016/j.engfracmech.2019.106629.

[33] Carreras L, Renart J, Turon A, Costa J, Essa Y, Martin de la Escalera F. An efficient methodology for the experimental characterization of mode II delamination growth under fatigue loading. Int J Fatigue 2017;95:185–93. https://doi.org/10.1016/J.IJFATIGUE.2016.10.017.

[34] Ballarin P, Airoldi A, Aceti P, Ghiasvand S, Sala G. Experimental Identification of Frictional Effects on Interlaminar Toughness of Composite Laminates in 4ENF Test. Exp Mech 2022;62:1135–45. https://doi.org/10.1007/s11340-022-00860-8.

[35] Pitarresi G, Scalici T, Catalanotti G. Thermoelastic Stress Analysis of modified Transverse Cut Tensile composite specimens under pure Mode II fatigue delamination. Procedia Structural Integrity 2018;8:474–85. https://doi.org/10.1016/j.prostr.2017.12.047.

[36] Brunner AJ, Stelzer S, Pinter G, Terrasi GP. Mode II fatigue delamination resistance of advanced fiber-reinforced polymer-matrix laminates: Towards the development of a standardized test procedure. Int J Fatigue 2013;50:57–62. https://doi.org/10.1016/j.ijfatigue.2012.02.021.

[37] Scalici T, Pitarresi G, Catalanotti G, van der Meer FP, Valenza A. The Transverse Crack Tension test revisited: An experimental and numerical study. Compos Struct 2016;158:144–59. https://doi.org/10.1016/j.compstruct.2016.09.033.

[38] Cui W, Wisnom MR, Jones M. An Experimental and Analytical Study of Delamination of Unidirectional Specimens with Cut Central Plies. Journal of Reinforced Plastics and Composites 1994;13:722–39. https://doi.org/10.1177/073168449401300804.

[39] Wisnom MR. On the Increase in Fracture Energy with Thickness in Delamination of Unidirectional Glass Fibre-Epoxy with Cut Central Plies. Journal of Reinforced Plastics and Composites 1992;11:897–909. https://doi.org/10.1177/073168449201100802.

[40] Pitarresi G, Scalici T, Catalanotti G. Infrared Thermography assisted evaluation of static and fatigue Mode II fracture toughness in FRP composites. Compos Struct 2019;226. https://doi.org/10.1016/j.compstruct.2019.111220.

[41] Hahn P, Channammagari H, Imbert M, May M. High-rate mode II fracture toughness testing of polymer matrix composites using the Transverse Crack Tension (TCT) test. Compos B Eng 2022;233:109636. https://doi.org/10.1016/j.compositesb.2022.109636.

[42] Hexcel Corporation. Product data sheet HexPly® | M79 UD600 2014.

[43] ASTM. A606 - Standard Specification for Steel, Sheet and Strip, High-Strength, Low-Alloy, Hot-Rolled and Cold-Rolled, with Improved Atmospheric Corrosion Resistance 2018.

[44] Hexcel Corporation. Product data sheet HexPly® | HexBond™ 679 2020.

[45] Blaber J, Adair B, Antoniou A. Ncorr: Open-Source 2D Digital Image Correlation Matlab Software. Exp Mech 2015;55:1105–22. https://doi.org/10.1007/s11340-015-0009-1.

[46] Fink A, Camanho PP, Andrés JM, Pfeiffer E, Obst A. Hybrid CFRP/titanium bolted joints: Performance assessment and application to a spacecraft payload adaptor. Compos Sci Technol 2010;70:305–17. https://doi.org/10.1016/j.compscitech.2009.11.002.

[47] Bao G, Ho S, Suo Z, Fan B. The role of material orthotropy in fracture specimens for composites. Int J Solids Struct 1992;29:1105–16. https://doi.org/10.1016/0020-7683(92)90138-J.

[48] Suo, Z; Bao, G; Fan, B; Wang TC. Orthotropy rescaling and implications for fracture in composites. Int J Solids Struct 1991;28:235–48.

[49] Dassault Systèmes. ABAQUS Documentation. Providence, RI: 2012.

[50] Krueger R. Virtual crack closure technique: History, approach, and applications. Appl Mech Rev 2004;57:109–43. https://doi.org/10.1115/1.1595677.

[51] ASTM. E8/E8M-22 - Standard Test Methods for Tension Testing of Metallic Materials 2022.

Figure Caption

Table Caption